$BiFeO_3$ Domain Wall Energies and Structures: A Combined Experimental and Density Functional Theory + U Study

Yi Wang,[1] Chris Nelson,[2] Alexander Melville,[3] Benjamin Winchester,[1] Shunli Shang,[1] Zi-Kui Liu,[1] Darrell G. Schlom,[3,4] Xiaoqing Pan,[2] and Long-Qing Chen[1]

[1]*Materials Science and Engineering, The Pennsylvania State University, University Park, Pennsylvania 16802, USA*
[2]*Department of Materials Science and Engineering, The University of Michigan, Ann Arbor, Michigan 48109, USA*
[3]*Department of Materials Science and Engineering, Cornell University, Ithaca, New York 14853, USA*
[4]*Kavli Institute at Cornell For Nanoscale Science, Ithaca, New York 14853, USA*

(Received 18 April 2013; published 24 June 2013)

We determined the atomic structures and energies of 109°, 180°, and 71° domain walls in $BiFeO_3$, combining density functional theory + U calculations and aberration-corrected transmission electron microscopy images. We find a substantial Bi sublattice shift and a rather uniform Fe sublattice across the walls. The calculated wall energies (γ) follow the sequence $\gamma_{109} < \gamma_{180} < \gamma_{71}$ for the 109°, 180°, and 71° walls. We attribute the high 71° wall energy to an opposite tilting rotation of the oxygen octahedra and the low 109° wall energy to the opposite twisting rotation of the oxygen octahedra across the domain walls.

DOI: 10.1103/PhysRevLett.110.267601 PACS numbers: 77.80.Dj, 68.37.Og, 77.55.Nv

Bismuth ferrite ($BiFeO_3$) is a room temperature, single-phase magnetoelectric multiferroic [1,2] characterized by a large spontaneous electric polarization of $\sim 100\ \mu C/cm^{-2}$, a ferroelectric transition Curie temperature of ~1120 K, and an antiferromagnetic transition Néel temperature of ~640 K. One of the signatures of all ferroic materials is the formation of domains below their ferroic transition temperatures, dictated by the crystallographic symmetry group and subgroup relations between the parent phase and the ferroic phase. Accordingly, many applications of ferroic materials, such as data storage, spintronics, and microelectronic devices, are achieved through the control and manipulation of their domain structures [3–5], each of them is a micro or nanoscale region with uniform spontaneous polarization, magnetization, or strain. The current interest in $BiFeO_3$ is the precise atomic structures and the domain wall energies of 109°, 180°, and 71° domain walls [6] between single crystal domains.

At room temperature, ferroelectric $BiFeO_3$ is a rhombohedrally distorted perovskite (space group $R3c$) with an inner angle (α_c) of 89°28'. Using the pseudocubic directions to describe the crystal directions and planes, the spontaneous polarization is along the $[111]_P$ axis [7–10]. The ferroelectric phase transition in $BiFeO_3$ also produces lattice distortions along the $\langle 111\rangle_P$ directions through electrostrictive effects, leading to four possible ferroelectric variants. Among the domain variants, there are three types of domain walls across which the polarization direction changes by 71°, 109°, or 180°. Despite extensive experimental and theoretical work on $BiFeO_3$ [11–14], the atomic structures and energies of domain walls in $BiFeO_3$ are not accurately known. In particular, Lubk *et al.* [15] and Seidel *et al.* [16] have previously constructed supercell models for these three domain walls of $BiFeO_3$. Their calculated 71° domain wall energy of 363 mJ/m^2 differs, however, by a factor of 4 from the value of 92 mJ/m^2 by Chen *et al.* [17] obtained using the phenomenological Landau-Ginzburg-Devonshire analysis by fitting the measured domain width and thin film thickness. Recent DFT (density functional theory) calculations by Ren *et al.* [18] show much lower domain wall energies than previously reported but in agreement with our reported values.

In this Letter, we present a combined experimental and density functional theory plus U (DFT + U) study of ferroelectric domain walls in $BiFeO_3$. Domain walls in 20 nm thick $BiFeO_3$ thin film grown on a (110) $TbScO_3$ substrate by reactive molecular-beam epitaxy were examined [19]. Spherical aberration (Cs)-corrected scanning transmission electron microscopy (STEM) is used to corroborate the domain wall structures from DFT + U calculations by comparing distortions of the Bi and Fe sublattices across each type of domain wall. The 109°, 180°, and 71° domain wall energies are then calculated. We employ the projector-augmented wave method [20,21] together with the rotationally invariant DFT + U method by Liechtenstein *et al.* [22] as implemented in the Vienna *ab initio* simulation package (VASP, version 5.2).

In addition to the *G*-type antiferromagnetic arrangements of Fe spins and Fe displacement from the cubic center, $BiFeO_3$ also shows counterrotation of oxygen octahedra, corresponding closely to the Fe spin-up and spin-down distributions, with the rotation axis along the pseudocubic $[111]_P$ axis. Therefore, in constructing supercell models for domain walls of $BiFeO_3$, two key factors affect the accuracy of the DFT calculations: (i) the equivalency of the two domain walls within the supercell in order to maintain charge neutrality and (ii) the local atomic

arrangement across the wall accounting for the changes of the canting of the oxygen octahedra.

To generate the supercell expression of the domain wall, we start by making a reference structure, which is a doubling of the 10-atom $R3c$ cell and a $\sqrt{2} \times \sqrt{2} \times 2$ superstructure of the 5-atom pseudocubic cell. Using the reference structure as a building block, the supercell models for the 109°, 180°, and 71° domain walls have been derived using twinlike operations with head-to-tail patterns. After DFT + U relaxation, the optimized structures are shown in Figs. 1(a), 2(a), and 3(a), respectively, for the 109°, 180°, and 71° domain walls.

The details about film growth can be found in the supplemental section of Ref. [19]. The θ–2θ scan suggests that the film is free of unwanted phases and completely aligned out of plane. The rocking curve scans show that the film and the substrate peak have approximately equal full-width at half-maximum values, suggesting that the film is commensurate to the substrate and of comparable single-crystalline quality. STEM imaging of the domain walls was performed at "room temperature," without active heating or cooling of the sample stage.

In our STEM measurement, the domain walls are characterized using high-angle annular dark field (HAADF) imaging with subangstrom resolution. This technique produces atomic scale "Z-contrast" images (Z = atomic number) where the apparent intensity of the projected atomic column scales by approximately Z^2 [19,23,24]. Figures 1(c) and 2(c) show Z-contrast images of the 109° domain wall viewed down the $[010]_P$ zone axis and the 180° domain wall viewed down the $[001]_P$ zone axis for a $BiFeO_3$ thin film. The domain walls are centered in the image (at $x = 0$) and oriented vertically in the plane of the paper. The 71°, 109°, and 180° domain walls are found to adopt $(001)_P$, $(110)_P$, and $(\bar{1}10)_P$ pseudocubic domain wall planes, respectively, in the $BiFeO_3$ film which correspond to expected low-energy planes. Unlike the 109° and 180° cases, the $(110)_P$ 71° domain walls cannot be viewed "edge on" (along the $[001]_P$ direction) as it is a single reversal along the $[001]_P$ direction. Therefore, atomic resolution Z-contrast imaging could not be used to verify the 71° domain wall structure. From measuring the polar displacement of the Bi sublattice at each atomic column the thickness of the 109° domain wall is found to be about one Fe column along the $[001]_p$ direction, and the thickness of the 180° domain wall is two Fe columns along the $[\bar{1}10]_P$ direction. In comparison, the previously measured domain wall widths [16,23] are substantially larger than in the present work. For example, Borisevich *et al.* [23] and Seidel *et al.* [16] showed that the 109° domain wall thickness were 5–7 pseudocubic unit cells.

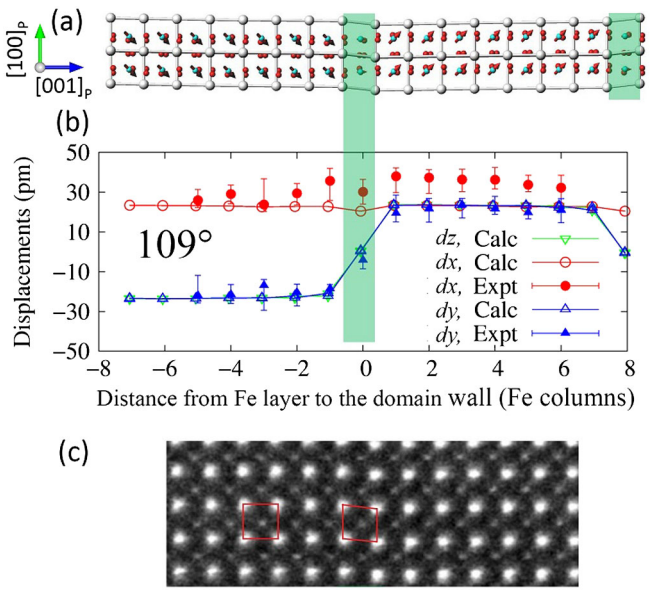

FIG. 1 (color online). Atomic structure of 109° domain wall in $BiFeO_3$. The domain wall regions are emphasized by the green shadows. (a) The calculated atomic positions and the displacement directions (red arrows) of the local Fe layers relative to the centers of the Bi sublattices. (b) The displacement (1 pm = 0.01 Å) of Fe layers relative to the centers of the Bi sublattices where the open symbols are from DFT + U calculation and the filled symbols are from the STEM measurements. (c) Z-contrast image.

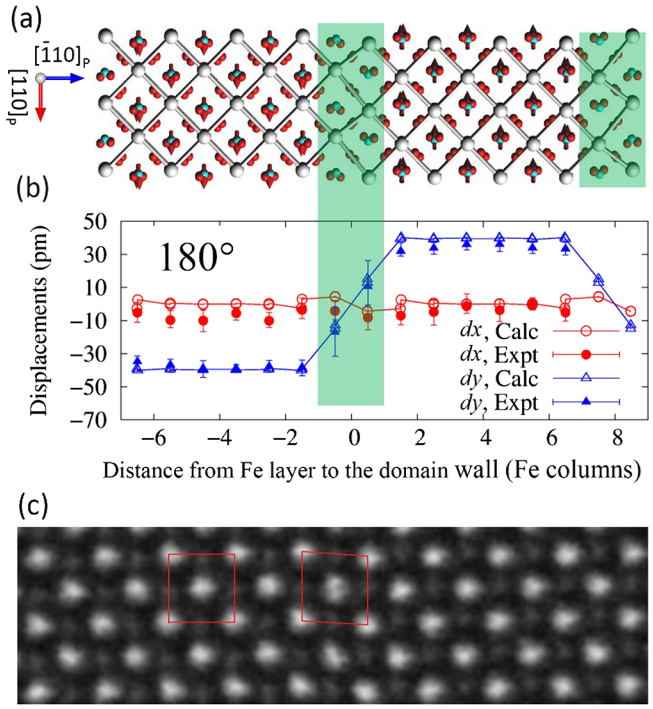

FIG. 2 (color online). Atomic structure of 180° domain wall in $BiFeO_3$. (a) The calculated atomic positions and the displacement directions (red arrows) of the local Fe layers relative to the centers of the Bi sublattices. (b) The displacement (1 pm = 0.01 Å) of Fe layers relative to the centers of the Bi sublattices where the open symbols are from DFT + U calculation and the filled symbols are from the STEM measurements. (c) Z-contrast image.

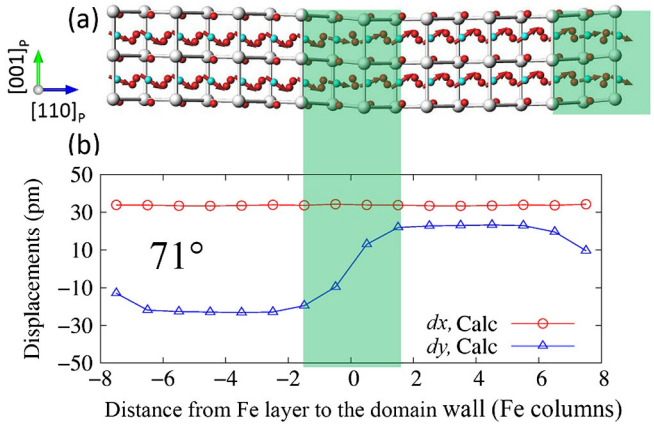

FIG. 3 (color online). Atomic structure of 71° domain wall in $BiFeO_3$. (a) The calculated atomic positions and the displacement directions (red arrows) of the local Fe layers relative to the centers of the Bi sublattices. (b) The displacement (1 pm = 0.01 Å) of Fe layers relative to the centers of the Bi sublattices obtained from DFT + U calculation.

The dominant polar displacement in bulk $BiFeO_3$ is that of the Bi cations from their corner positions of the psuedocubic unit cell. The local Bi displacement relative to the Fe sublattice can therefore be used to determine the polarization vector [19]. This is evident in the Z-contrast images of Fig. 1(c) (a 109° domain wall) and Fig. 2(c) (a 180° domain wall) in the sudden offset of the Bi sublattice ($Z = 83$, bright atoms) at the domain wall compared to the uniform Fe sublattice throughout the image ($Z = 26$, darker atoms). This local shearing deformation of the Bi sublattice at the domain wall is highlighted in both images by comparing the Bi-corner unit cells within the domain and at the domain wall (red boxes). The x and y components of the Fe offset relative to Bi are shown in Figs. 1(b) and 2(b) (closed symbols with error bars) as a function of distance normal to the domain wall (x) for both 109° and 180° domain walls. The values correspond to the median value of the Fe cation offset relative to the center of mass of its 4 nearest Bi neighbors and sample >20 unit cells parallel to the domain wall. The 109° domain wall consists of only a single transitional Fe atomic column whereas the 180° domain wall spans two transitional Bi/Fe atomic columns. For the 180° domain wall, the change in displacement occurs almost entirely parallel to the domain wall plane (dy, $[110]_p$ pseudocubic direction in Fig. 2). For the 109° domain wall, only the change in displacement parallel to the $[100]_p$ pseudocubic direction (dy, Fig. 1) can be measured. For both the 109° and 180° domain walls, the observed displacement normal to the domain wall (dx) remains roughly constant, maintaining the charge neutrality.

A comparison of the calculated atomic positions using the 160-atom supercells with the experimentally measured data in Figs. 1 and 2 for the 109° and 180° domain walls, respectively, shows excellent agreement. Qualitatively the experimental data and the DFT + U calculations exhibit similar deformation of the Bi sublattice (region highlighted in green). The calculated directional changes in the Fe cation displacement relative to its eight nearest Bi neighbors as a function of distance to the domain wall are marked in Figs. 1(a), 2(a), and 3(a) for the 109°, 180°, and 71° domain walls, respectively.

A quantitative comparison between the experimental data and the DFT + U calculations is made by calculating the displacement of the ith Fe cation relative to its eight nearest Bi neighbors according to

$$\mathbf{D}(i) = \mathbf{R}_{\mathrm{Fe}}(i) - \frac{1}{8}\sum_{k=1}^{8}\mathbf{R}_{\mathrm{Bi}}(k),$$

where $\mathbf{R}_{\mathrm{Fe}}$ and $\mathbf{R}_{\mathrm{Bi}}$ represent the atomic positions for Fe and Bi atoms, respectively, after fully relaxing the supercell.

Figures 1(b) and 2(b) show numerical comparisons between the calculations and the HAADF imaging for 109° and 180° domain walls. In particular, within the 109° domain wall, we see a transition layer containing only one Fe column where the x component (labled dx in the figures) of the Fe displacement relative to the center of the Bi sublattice is roughly the same as that of the bulk, while the y component (labeled dy in the figures) of the Fe displacement relative to the center of the Bi sublattice is roughly zero. Within the 180° domain wall, we see a transition layer containing two Fe columns where dx is almost the same as that of the bulk, while dy is about 1/4 of that of the bulk. Within the 71° domain wall (Fig. 3), we see a transition layer containing 2–4 Fe columns where dx is approximately the same as the bulk, while dy is a little over half of that of the bulk.

The calculated domain wall energies from the present work with the 160-atom supercells are 128, 33, and 98 $\mathrm{mJ/m^2}$ for the 71°, 109°, and 180° domain walls, respectively. While the wall energy that we calculated for the 71° wall is close to the estimated value of 92 $\mathrm{mJ/m^2}$ by Chen *et al.* [17], the wall energy we calculated for the 180° domain wall is over 5 times lower than the value of 829 $\mathrm{mJ/m^2}$ of prior calculations [15,16] and the values of 687–956 $\mathrm{mJ/m^2}$ of the thermodynamic analysis [23]. There are a number of possible reasons for the disagreements between the present results and those by Lubk *et al.* [15] and Seidel *et al.* [16]: First, for a supercell calculation of domain wall energies, two domain walls in a supercell should be equivalent in order to maintain charge neutrality. The two domain walls in each supercell in this work are equivalent whereas among those constructed by Lubk *et al.* [15], only the 109° domain wall supercell possesses two equivalent domain walls. Further, the local atomic arrangements near the 109° and 71° domain walls in our supercells are similar to those by Lubk *et al.* while for the 180° domain wall the atomic positions near the domain walls in our supercell differ substantially from those of Lubk *et al.*

Second, since a supercell contains two domain walls, a factor of 1/2 needs to be applied to the domain wall energies calculated by Lubk *et al.* and Seidel *et al.* Finally, the different calculation schemes, general gradient approximation plus U in this work (see the Supplemental Material [26]) and the local spin density approximation plus U by Lubk *et al.* may yield somewhat different results.

We note that our calculated domain wall energies for $BiFeO_3$ are quite comparable to those previously calculated for $PbTiO_3$ by Meyer and Vanderbilt [25] and two very recent calculations [18,27]. The two systems only have 180° domain walls in common and the comparison is 98 mJ/m^2 for $BiFeO_3$ versus 128 mJ/m^2 for $PbTiO_3$ [25]. The 33 mJ/m^2 that we calculated for the low energy 109° $BiFeO_3$ domain wall is also very close to the 35 mJ/m^2 of the 90° $PbTiO_3$ domain wall [25]. The sequence of domain wall energies is also consistent with indirect experimental observation [19] that $BiFeO_3$ films form 109° domain walls instead of 180° domain walls. Furthermore, in vortex domains 180° domain walls are observed rather than 71° domain walls [19].

In our DFT + U calculations, the 71° domain wall is predicted to have the highest interfacial energy and the 109° domain wall is predicted to have the lowest. This is somewhat counterintuitive according to the Ginzburg-Landau analysis [23] which says that the 180° domain wall should be the highest. Lubk *et al.* [15] have previously determined this trend results from the ability of the domain wall planes to accommodate distortions by the canting of the oxygen coordination octahedra [15]. In order to compare the changes and distortions by the canting of the oxygen octahedra across the 71°, 109°, and 180° domain walls, we plot the calculated oxygen octahedral rotation in Fig. 4. The rotation angles are defined with respect to the [100], [010], and [001] directions of the cubic phase. For single crystal $R3c$ $BiFeO_3$ without domain walls, the rotation angles with respect to the [100], [010], and [001] axes are identical (~8°) by our calculation. The changes of the canting of the oxygen octahedra for the highest energy domain wall, 71°, exhibits the opposite tilting rotation of the oxygen octahedra across its domain wall, with the change by the rotation axis [the [001] axis in Fig. 4(a)] being parallel to the domain wall. In contrast, the changes of the canting of the oxygen octahedra for the lowest energy domain wall, 109°, exhibits an opposite twisting rotation of the oxygen octahedra, with the change by the rotation axis [the [001] axis in Fig. 4(b)] being perpendicular to the domain wall. These types of changes of the rotations occur because the octahedra are corner shared along the $(100)_P$ pseudocubic domain wall plane which allows them to easily change rotation without being otherwise distorted. Based on the changes in the oxygen octahedral rotation across the domain walls, the width of 109° domain wall is significantly smaller than the 71° domain wall. In contrast to both the 71° and 109° walls, adjacent

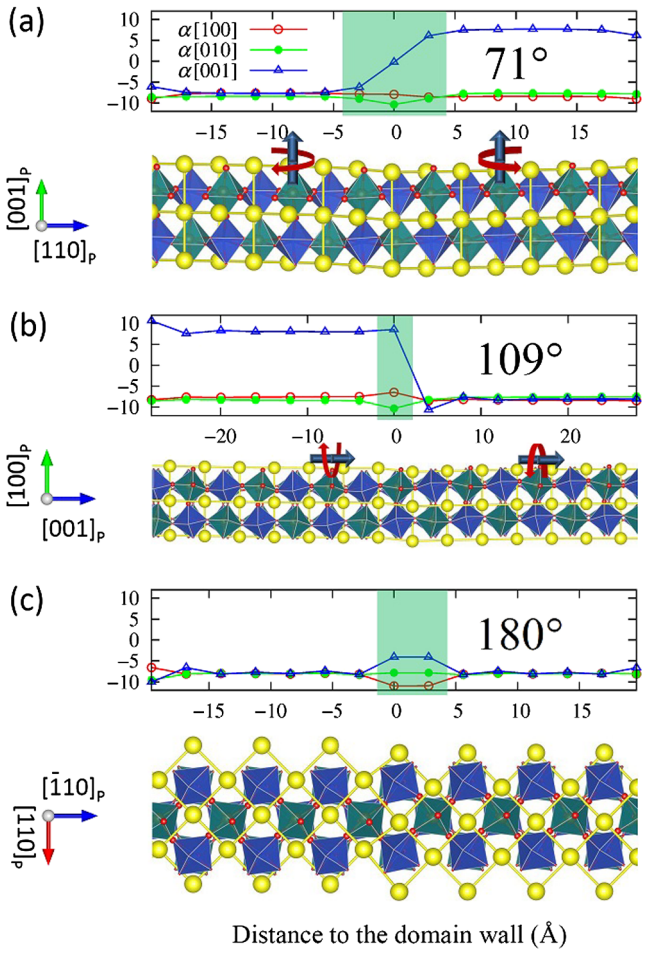

FIG. 4 (color online). Oxygen octahedral rotation across (a) 71°, (b) 109°, and (c) 180° domain walls. The side domain wall regions are cropped. The rotation angles (point-line plots) are only shown for the octahedra containing spin-up Fe atoms. For the (a) 71° and (b) 109° walls, the oxygen octahedral rotations are labeled with rotation symbols for selected octahedra to emphasize the changes in rotation across the domain walls.

domains across a 180° domain wall have roughly the same octahedral canting angle. There is, however, still a local distortion spanning more than two oxygen octahedra across the 180° domain wall. Therefore, a Ginzburg-Landau theory incorporating both polarization and ferrodistortive order as order parameters is required to quantitatively describe the relative energies of domain walls in $BiFeO_3$.

In summary, the structures and energies of $BiFeO_3$ domain walls have been studied using a combination of HAADF imaging and DFT + U calculations. Both the calculation and the measurement show that across the domain walls the Fe sublattice is relatively uniform and the Bi sublattice shows a substantial shift, implying that the change in polarization is due to the shift of the Bi sublattice. The oxygen octahedral rotation changes across the three types of walls correspond to the thicknesses obtained

by analyzing the atomic displacement distributions from both the DFT + U calculations and HAADF images.

This work is supported by the U.S. Department of Energy, Office of Basic Energy Sciences, Division of Materials Sciences and Engineering under Award DE-FG02-07ER46417 (Y. W., B. W., and L.-Q. C.) and DOE DE-FG02-07ER46416 (C. N. and X. P.), DMR-0723032 (aberration-corrected TEM instrument), and in part supported by instrumentation (cyberstar Linux cluster) funded by the National Science Foundation through Grant No. OCI-0821527. The work at Cornell was supported by Army Research Office (ARO) Grant No. W911NF-08-2-0032. B. W. was supported by Penn State and MRSEC under Grant No. MRSEC DMR-0820404. Calculations were conducted at the National Energy Research Scientific Computing Center, which is supported by the Office of Science of the U.S. Department of Energy under Contract No. DE-AC02-05CH11231. The authors would also like to acknowledge the National Center for Electron Microscopy at Lawrence Berkeley National Laboratory for their support under the DOE Grant No. DE-AC02-05CH11231 for user facilities. Dr. Lubk and Professor Spaldin are especially acknowledged for kindly offering their atomic position files.

[1] D. Lebeugle, D. Colson, A. Forget, and M. Viret, Appl. Phys. Lett. **91**, 022907 (2007).
[2] D. Lebeugle, D. Colson, A. Forget, M. Viret, A. M. Bataille, and A. Gukasov, Phys. Rev. Lett. **100**, 227602 (2008).
[3] N. Balke, B. Winchester, W. Ren, Y. H. Chu, A. N. Morozovska, E. A. Eliseev, M. Huijben, R. K. Vasudevan, P. Maksymovych, J. Britson, S. Jesse, I. Kornev, R. Ramesh, L. Bellaiche, L. Q. Chen, and S. V. Kalinin, Nat. Phys. **8**, 81 (2011).
[4] G. Catalan, J. Seidel, R. Ramesh, and J. F. Scott, Rev. Mod. Phys. **84**, 119 (2012).
[5] A. Roy, R. Gupta, and A. Garg, Adv. Condens. Matter Phys. **2012**, 926290 (2012).
[6] C. A. Randall, D. J. Barber, and R. W. Whatmore, J. Mater. Sci. **22**, 925 (1987).
[7] C. Ederer and N. A. Spaldin, Phys. Rev. Lett. **95**, 257601 (2005).
[8] J. Wang, J. B. Neaton, H. Zheng, V. Nagarajan, S. B. Ogale, B. Liu, D. Viehland, V. Vaithyanathan, D. G. Schlom, U. V. Waghmare, N. A. Spaldin, K. M. Rabe, M. Wuttig, and R. Ramesh, Science **299**, 1719 (2003).
[9] R. R. Das, D. M. Kim, S. H. Baek, C. B. Eom, F. Zavaliche, S. Y. Yang, R. Ramesh, Y. B. Chen, X. Q. Pan, X. Ke, M. S. Rzchowski, and S. K. Streiffer, Appl. Phys. Lett. **88**, 242904 (2006).
[10] J. F. Li, J. L. Wang, M. Wuttig, R. Ramesh, N. Wang, B. Ruette, A. P. Pyatakov, A. K. Zvezdin, and D. Viehland, Appl. Phys. Lett. **84**, 5261 (2004).
[11] A. Lubk, M. D. Rossell, J. Seidel, Q. He, S. Y. Yang, Y. H. Chu, R. Ramesh, M. J. Hytch, and E. Snoeck, Phys. Rev. Lett. **109**, 047601 (2012).
[12] S. Prosandeev, I. A. Kornev, and L. Bellaiche, Phys. Rev. Lett. **107**, 117602 (2011).
[13] D. Rahmedov, D. W. Wang, J. Iniguez, and L. Bellaiche, Phys. Rev. Lett. **109**, 037207 (2012).
[14] Y. R. Yang, W. Ren, M. Stengel, X. H. Yan, and L. Bellaiche, Phys. Rev. Lett. **109**, 057602 (2012).
[15] A. Lubk, S. Gemming, and N. A. Spaldin, Phys. Rev. B **80**, 104110 (2009).
[16] J. Seidel, L. W. Martin, Q. He, Q. Zhan, Y. H. Chu, A. Rother, M. E. Hawkridge, P. Maksymovych, P. Yu, M. Gajek, N. Balke, S. V. Kalinin, S. Gemming, F. Wang, G. Catalan, J. F. Scott, N. A. Spaldin, J. Orenstein, and R. Ramesh, Nat. Mater. **8**, 229 (2009).
[17] Y. B. Chen, M. B. Katz, X. Q. Pan, R. R. Das, D. M. Kim, S. H. Baek, and C. B. Eom, Appl. Phys. Lett. **90**, 072907 (2007).
[18] W. Ren, Y. Yang, O. Diéguez, J. Íñiguez, N. Choudhury, and L. Bellaiche, Phys. Rev. Lett. **110**, 187601 (2013).
[19] C. T. Nelson, B. Winchester, Y. Zhang, S. J. Kim, A. Melville, C. Adamo, C. M. Folkman, S. H. Baek, C. B. Eom, D. G. Schlom, L. Q. Chen, and X. Q. Pan, Nano Lett. **11**, 828 (2011).
[20] P. E. Blöchl, Phys. Rev. B **50**, 17 953 (1994).
[21] G. Kresse and D. Joubert, Phys. Rev. B **59**, 1758 (1999).
[22] A. I. Liechtenstein, V. I. Anisimov, and J. Zaanen, Phys. Rev. B **52**, R5467 (1995).
[23] A. Borisevich, O. S. Ovchinnikov, H. J. Chang, M. P. Oxley, P. Yu, J. Seidel, E. A. Eliseev, A. N. Morozovska, R. Ramesh, S. J. Pennycook, and S. V. Kalinin, ACS Nano **4**, 6071 (2010).
[24] B. Rafferty and S. J. Pennycook, Ultramicroscopy **78**, 141 (1999).
[25] B. Meyer and D. Vanderbilt, Phys. Rev. B **65**, 104111 (2002).
[26] See Supplemental Material at http://link.aps.org/supplemental/10.1103/PhysRevLett.110.267601 for more computational details of our calculations.
[27] O. Diéguez, P. Aguado-Puente, J. Junquera, and J. Íñiguez, Phys. Rev. B **87**, 024102 (2013).